



Technical Note

# Equidistant Nodes Orthogonal Polynomial Fitting for Harmonic Constants of Long-Period Tides Based on Satellite Altimeter Data

Yunfei Zhang <sup>1</sup>, Qixiang Wang <sup>1</sup> , Yibo Zhang <sup>1</sup> , Minjie Xu <sup>2</sup>, Yonggang Wang <sup>3,4,\*</sup> and Xianqing Lv <sup>1</sup>

<sup>1</sup> Frontier Science Center for Deep Ocean Multispheres and Earth System (FDOMES) and Physical Oceanography Laboratory, Ocean University of China, Qingdao 266100, China; zhangyunfei@stu.ouc.edu.cn (Y.Z.)

<sup>2</sup> School of Ocean, Yantai University, Yantai 264005, China

<sup>3</sup> Laboratory for Regional Oceanography and Numerical Modeling, Pilot National Laboratory for Marine Science and Technology, Qingdao 266237, China

<sup>4</sup> First Institute of Oceanography, and Key Laboratory of Marine Science and Numerical Modeling, Ministry of Natural Resources, Qingdao 266061, China

\* Correspondence: ygwang@fio.org.cn

**Abstract:** The harmonic constants of long-period tidal constituents are critical for simulating the tide process, obtaining theoretical datum sounding reduction, and conducting further ocean research. In this paper, the equidistant node orthogonal polynomial fitting (ENOPF) method is employed to fit the harmonic constants of the T/P satellite altimeter data and the gridded altimeter data from the Data Unification and Altimeter Combination System (DUACS) to obtain the full-field harmonic constants of the long-period tidal constituents ( $S_a$  and  $S_{sa}$ ) in the Bohai Sea, Yellow Sea, and East China Sea (BYECS). To verify the validity of the ENOPF method, the long-period tidal harmonic constants of the ENOPF method, the Finite Element Solutions 2014 (FES2014) model, the Empirical Ocean Tide 20 (EOT20) model, and the DUACS data were compared with the observations of the X-TRACK products and the tide gauges. In addition, the root-mean-square errors (RMSEs), amplitude differences ( $\Delta H$ ), and phase-lag differences ( $\Delta G$ ) of the comparison results were calculated. According to the error analysis and the cotidal charts, the ENOPF method is better than the other three methods or models for comparing tide gauges (6.19 cm, 5.85 cm, 25.44°; 1.10 cm, 0.72 cm, 59.09°, respectively). The cotidal charts obtained by the ENOPF method are smoother and have better consistency with the actual track data. The results indicate that, due to the polynomial fitting method adopted in ENOPF method, which has the characteristics of improving the resolution infinitely, it is easier to obtain the harmonic constant of full field than with other models or methods. This study proves that the ENOPF method is a reasonable and simple tool in extracting the harmonic constants of the BYECS.

**Keywords:** equidistant node orthogonal polynomial fitting; satellite observation; data analysis; tidal harmonic constants; long-period tidal constituents



**Citation:** Zhang, Y.; Wang, Q.; Zhang, Y.; Xu, M.; Wang, Y.; Lv, X.

Equidistant Nodes Orthogonal Polynomial Fitting for Harmonic Constants of Long-Period Tides Based on Satellite Altimeter Data. *Remote Sens.* **2023**, *15*, 3246.

<https://doi.org/10.3390/rs15133246>

Academic Editor: Sergei Badulin

Received: 5 May 2023

Revised: 14 June 2023

Accepted: 20 June 2023

Published: 23 June 2023



**Copyright:** © 2023 by the authors. Licensee MDPI, Basel, Switzerland. This article is an open access article distributed under the terms and conditions of the Creative Commons Attribution (CC BY) license (<https://creativecommons.org/licenses/by/4.0/>).

## 1. Introduction

A tide is a basic form of ocean movement that has a crucial impact on ocean phenomena such as waves, ocean currents, and storm surges [1]. In estuarine and coastal systems, the transport and mixing of sediment, nutrients, and organisms are often affected by tidal processes [2]. Furthermore, the tidal current is a significant form of seawater movement in the shelf ocean. Fang (1979) estimated that the average wind-induced wave energy in the Yellow Sea is only one-seventh of the energy of the  $M_2$  tidal current, and the energy of the residual current is smaller [3]. The tidal current not only plays an important role in ocean engineering and ecological environment but also has an important impact on various processes in the ocean, such as ocean stratification, fronts, currents, sediment movement, and pollutant destination [4]. The tide and tidal current both have an impact on

the significant wave height, which is the main factor in the prediction of waves and ocean dynamics [5–7]. Accurate ocean tidal simulation is an important basis for the studies of other marine and geophysical phenomena which use tidal data [3].

For the Bohai Sea, Yellow Sea, and East China Sea (BYECS) area, there are many numerical simulation studies on the eight major tidal constituents [8–11]. Some researchers regarded the BYECS as a whole study area and numerically simulated the height of the tide and analyzed its variation rule [12–14]. Kuh Kang used a high-resolution two-dimensional nonlinear tidal wave model to simulate the five major constituents of  $M_2$ ,  $S_2$ ,  $K_1$ ,  $O_1$ , and  $N_2$  and the shallow constituents of  $M_4$  and  $MS_4$  in the BYECS [15]. For the shallow-water tidal constituents, a numerical adjoint model was established using TOPEX/POSEIDON (T/P) satellite altimeter data to study the shallow-water tidal constituents in the Bohai Sea and the Yellow Sea [16,17]. However, there are still some shortcomings in these numerical simulation studies. It takes a large computational cost to obtain the harmonic constant with a  $15' \times 15'$  resolution or even higher.

The precise tidal harmonic constant is indispensable for numerical simulation and plays a critical role in predicting tide and determining the tidal datum plane [18]. Before the availability of satellite altimeter data, the cotidal charts of the Bohai Sea and the Yellow Sea were based on observations from coastal and island tide gauges. For example, Guo obtained the cotidal charts of the  $M_2$  and  $K_1$  constituents and the maximum tide velocity distribution of the two constituents based on hundreds of tide gauge observations and numerical simulation results [19]. However, because only the tide gauges offshore were fitted, the accuracy of tidal harmonic constants in the middle of the Bohai Sea and the Yellow Sea needs to be improved. TOPEX/Poseidon (T/P), launched in August 1992, provided high precision and extensive coverage of observational data. With the satellite altimeter data along the track, the more accurate tidal harmonic constant can be obtained by a harmonic analysis and response analysis [20,21]. In offshore areas, the accuracy of altimeter observations is relatively low due to the low resolution of ocean responses to tidal and atmospheric loads. Thus, the application of the satellite altimeter data analysis becomes more difficult in the offshore area than in the pelagic area. To solve the problem of low accuracy, the X-TRACK tidal harmonic constant product was invented as an improved altimeter product [22–24]. The Finite Element Solutions 2014 (FES2014) model and the EOT20 model were introduced to improve the accuracy of measurement, too [25,26]. However, the establishment of these models is relatively complicated, and the resolution can be further improved, which prompts us to search for a brief and effective method to obtain more accurate harmonic constants.

For the offshore areas, except for the eight major tidal constituents, the influence of the long-period tidal constituents cannot be ignored. The long-period tidal constituents can regulate the flattening of the Earth and, thus, its moment of inertia, so it is one of the most significant of the many factors affecting the rotation rate of the Earth and, thus, the length of day (LOD) [27]. By studying the long-period tidal constituents, we can measure the related parameters that affect the axial rotation of the Earth and then make more extensive geophysical inferences [28–30], which are indispensable to the research of theoretical sea level datum and other fields. Ray and Eroffeva (2014) built a model of long-period tidal variations in the length of the day; the model eliminates the disadvantage that the original model had from leaving significant residual tidal energy [27]. Kantha et al. (1998) used a barotropic global hydrodynamic tidal mode to extract the long-period tides in the ocean [31]. Observations of long-period tides can provide valuable information on how the ocean reacts to external forcing and energy dissipation, because the forcing of long-period tides is well-known, albeit limited to a narrow frequency and wavenumber range; it can also help us to analyze long-term sea-level change, which is an important factor in clarifying the physical processes in the ocean [32,33]. By applying a stratified equation model, and in the presence of an atmospherically forced ocean general circulation, the dynamic response characteristics of long-period tides under various conditions are explored [29]. In this research, the  $S_a$  and  $S_{sa}$  tides constituents of the long-period tides were selected for study

because the amplitudes of the  $S_a$  and  $S_{sa}$  are larger and the tide-gauge data are more complete than others, and they are not only related to astronomical forcing but also to meteorological phenomena. However, compared with the eight major tidal constituents, the long-period tidal constituents ( $S_a$  and  $S_{sa}$ ) have a longer period and smaller amplitude, so the harmonic constants of the long-period tidal constituents are difficult to obtain, and due to the characteristics of the long period, the harmonic constants obtained by using various models is limited by the computational data and capacity, and the selection of the open boundary conditions is also more difficult, so that the resolution of the obtained harmonic constants is not accurate enough to carry out any further study.

This study employed a simple and effective method, the equidistant node orthogonal polynomial fitting (ENOPF) method, to obtain more accurate harmonic constants of the long-period tidal constituents. The equidistant nodes orthogonal polynomial fitting method has been proven to be effective in the eight major tidal constituents and has been successfully used in Hawaii, the Bohai Sea, and the Yellow Sea area [34–36]. Fitting by orthogonal polynomials cannot only avoid the ill-condition caused by too many polynomials but also easily obtain the data used for fitting [37,38].

In this paper, the ENOPF method is introduced in Section 2. Section 3 shows the cotidal charts of the Bohai Sea and the East China Sea and the comparative analysis results with other institutions and indicators. Section 4 highlights some conclusions and discusses the effectiveness of the long-period tidal harmonic constants obtained by the ENOPF method.

## 2. Data and Methods

### 2.1. Study Region and Data

The study region is 117.5–131°E, 24–41°N; it is located in the China Sea, and it represents a surface area of 1.25 million km<sup>2</sup>. Due to the combined effects of large tidal energy input and enhanced bottom friction associated with shallow shelf topography, regional tidal features have complex structures. The drastic changes in topography and water depth, as well as the obvious difference in the tidal characteristics of shallow water and deep water, result in different tides in shallow water (average water depth less than 100 m) and deep water (average water depth more than 300 m). Therefore, the study region of this paper is divided into two parts, Area I (117.5–131°E, 24–35°N) and Area II (117.5–131°E, 34–41°N), as shown in Figure 1, which also shows the distribution of the water depth in gradations of blue, ranging from 0 to more than 3000 m; the tracks of altimetry satellite (white line); and 62 tide gauge stations (red dots) throughout the BYECS. In the different areas, the different fitting schemes (with different fitting orders) are applied to fit the harmonic constant of the long-period tide. The tide gauge data were provided by actual measurement data, which could provide a precise harmonic constant.

The 47,446 tidal harmonic constants used to fit are from the T/P satellite altimeter data and the gridded altimeter data with a resolution of 15' × 15' of the Data Unification and Altimeter Combination System (DUACS). The Finite Element Solutions 2014 (FES2014) model and the EOT20 model are used to verify the accuracy of the ENOPF method. The FES2014 model is the latest version of the FES series of tidal prediction work, which is based on the hydrodynamic model of the tides and coupled to the ensemble data-assimilation code [25]. With the continuous improvement of accuracy in coastal areas and the promotion of the FES2014 model, the latest empirical tidal model, EOT20, was introduced [26]. The FES2014, the EOT20 model, and the DUACS models have been corrected by conventional altimeter corrections, so the harmonics constants obtained by these models do not include dynamic height variations and the steric height changes, only related to tidal changes. The FES2014, the EOT20 model, and the DUACS data perform the same error analysis as the ENOPF method. The results obtained by the four products were compared with the tide gauges and the X-TRACK data. The X-TRACK was proposed specifically for coastal measurements of sea surface height, mean sea surface height, or sea level anomalies. It adopted new data-filtering strategies and filtering techniques so that more valid data could be presented, and it selected local tidal simulations in the nearshore area, which, in turn,

improved the accuracy of the data in the coastal area [22,23]. The X-TRACK provides measured satellite remote-sensing data and significantly improves the result obtained in various coastal areas, which can provide sufficiently accurate harmonic constants, so the X-TRACK can be used as a criterion to estimate the results of the methods and models at the satellite observation points. The X-TRACK amplitude data and the X-TRACK phase-lag data of integrating and analyzing over a period are shown in Figure 2. These data were developed by the CTOH group at LEGOS, and they are now distributed by Archiving, Validation, and Interpretation of Satellite Oceanographic (AVISO+). The time span of the data is approximately 1993–2015.

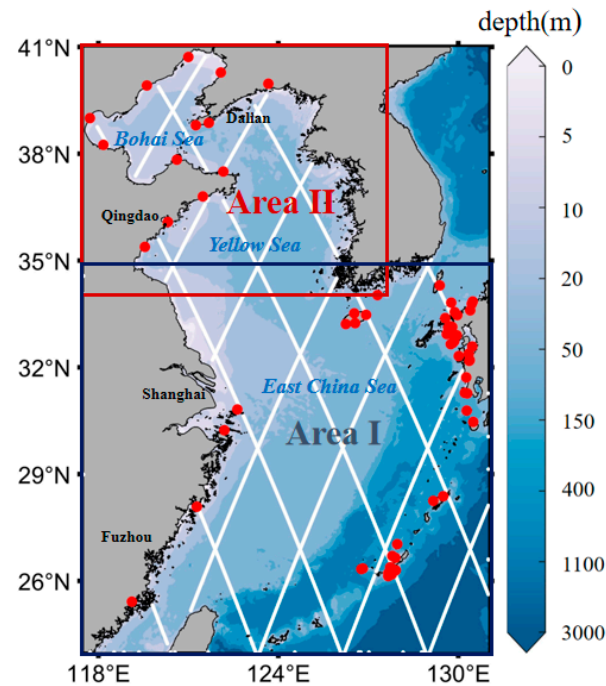


**Figure 1.** Two separate study areas divided by average water depth and distribution of the water depth in gradations of blue, ranging from 0 to more than 3000 m; the tracks of altimetry satellite (white line); and 62 tide gauge stations (red dots).

## 2.2. Methods

The equidistant node orthogonal polynomial fitting (ENOPF) method is employed to obtain the harmonic constants of the  $S_a$  and  $S_{sa}$  constituents. This method is based on satellite altimeter data and mostly affected by longitude and latitude orders ( $m$  and  $n$ ), which are the orders of equidistant node orthogonal polynomial, where the uncertain parameters such as water depth and bottom friction coefficient need not be considered. Furthermore, the ENOPF method is characterized by improving the resolution infinitely. The harmonics constants,  $H$  and  $G$ , for the long-period tidal constituents can be defined as follows:

$H$ : The harmonics constant that describes the amplitude of the tides. It represents the amplitude of the primary long-period constituent.  $G$ : The harmonics constant that describes the phase of the long-period tides relative to the mean sea level. It represents the phase lag of the primary long-period constituent.

To avoid the complex calculation of the fitting phase lag, the ENOPF method is used to fit the values of  $f = H\cos G$  and  $g = H\sin G$ .

For a set of  $n + 1$  isometric nodes  $\xi_i (i = 0, 1, \dots, n)$ , their step size is  $h$ , and the weight function is  $w_i = 1$ , using the following transformation:

$$x = \frac{\xi_i - \xi_0}{h} \quad (1)$$

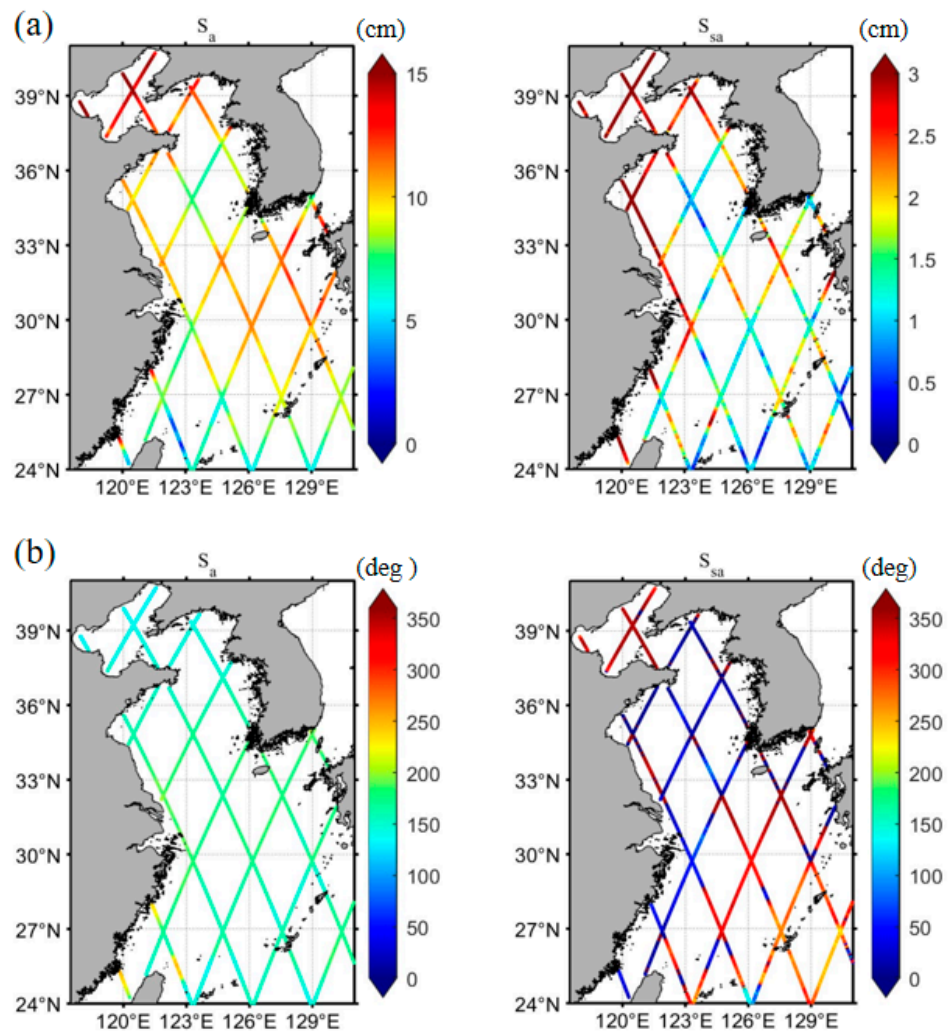


Figure 2. (a) X-TRACK amplitude data. (b) X-TRACK phase-lag data.

Then, the isometric nodes,  $\xi_i$ , will become  $x = 0, 1, 2, \dots, n$  of  $n + 1$  integer points. Considering the orthogonal property in the summation case, the power function,  $x^k$ , which is used to form the  $m$ -degree polynomial, should be replaced by the factorial product,  $x^{(k)}$ :

$$P_{m,n}(x) = 1 + b_1x + b_2x^{(2)} + \dots + b_mx^{(m)}, m < n \tag{2}$$

where  $x^{(m)} = x(x - 1) \dots (x - m + 1)$   $b_i$  is the coefficient of  $P_{m,n}(x)$ . To constitute a complete orthogonal system, the factorial product  $(x + k)^{(k)} (k = 0, 1, \dots, m - 1)$  of  $P_{m,n}(x)$  lower than  $m$  times must meet.

$$\sum_{x=0}^n (x + k)^{(k)} P_{m,n}(x) = 0 \tag{3}$$

$$P_{m,n}(x) = \sum_{k=0}^m (-1)^k \binom{m}{k} \binom{m+k}{k} \frac{x^{(k)}}{n^{(k)}} \tag{4}$$

It can also be proved that  $P_{m,n}(x)$  is a polynomial of degree  $m$  that satisfies the formula above the orthogonal condition, and its first several polynomials are as follows:

$$\begin{aligned}
 P_{0,n}(x) &= 1 \\
 P_{1,n}(x) &= 1 - 2\frac{x}{n} \\
 P_{2,n}(x) &= 1 - 6\frac{x}{n} + 6\frac{x(x-1)}{n(n-1)} \\
 P_{3,n}(x) &= 1 - 12\frac{x}{n} + 30\frac{x(x-1)}{n(n-1)} - 20\frac{x(x-1)(x-2)}{n(n-1)(n-2)} \\
 P_{4,n}(x) &= 1 - 20\frac{x}{n} + 90\frac{x(x-1)}{n(n-1)} - 140\frac{x(x-1)(x-2)}{n(n-1)(n-2)} + \\
 &\quad 70\frac{x(x-1)(x-2)(x-3)}{n(n-1)(n-2)(n-3)} \\
 P_{5,n}(x) &= 1 - 30\frac{x}{n} + 210\frac{x(x-1)}{n(n-1)} - 560\frac{x(x-1)(x-2)}{n(n-1)(n-2)} + \\
 &\quad 630\frac{x(x-1)(x-2)(x-3)}{n(n-1)(n-2)(n-3)} - 252\frac{x(x-1)(x-2)(x-3)(x-4)}{n(n-1)(n-2)(n-3)(n-4)}
 \end{aligned} \tag{5}$$

The polynomial family  $P_{m,n}(x)$  is a family of orthogonal polynomials, for which the weight function is 1 at  $x = 0, 1, 2, \dots, n$  of  $n + 1$  point.

For a two-dimensional rectangular field, the corresponding equidistant nodal orthogonal polynomials are as follows:

$$\begin{cases}
 D(x, y) = \sum_{k=0}^m \sum_{s=0}^n B_{k,s} T_{k,j}(x) P_{s,j}(y) \\
 T_{k,j}(x) = \sum_{i=0}^k (-1)^i \binom{k}{i} \binom{k+i}{i} \frac{x^{(i)}}{j^{(i)}} \\
 P_{s,j}(y) = \sum_{i=0}^s (-1)^i \binom{s}{i} \binom{s+i}{i} \frac{y^{(i)}}{j^{(i)}}
 \end{cases} \tag{6}$$

In Equation (6),  $B_{k,s}$  is the coefficient of equidistant node orthogonal polynomial with the orders  $k$  and  $s$ , which can be calculated by the least squares method;  $m$  and  $n$  are the orders of equidistant node orthogonal polynomial; and  $D(x, y)$  is the function value, which is the approximation of  $f$  or  $g$  at  $(x, y)$ . The amplitude,  $H$ , and phase lag,  $G$ , can be obtained by the following calculation:

$$\begin{aligned}
 H &= \sqrt{f^2 + g^2}, \\
 G &= \arctan(g/f).
 \end{aligned} \tag{7}$$

In this study, the DUACS and T/P satellite altimeter data are collated into the same form and put into a fitting procedure of the ENOPF method to obtain  $H$  and  $G$ . In the ENOPF method, different values of  $m$  and  $n$  would lead to different fitting results. Although the observed harmonic constants fitted with the larger  $m$  and  $n$  can obtain higher-accuracy results at the fitted points, too large an  $m$  and  $n$  may cause overfitting, which could generate a large error at the non-observation point. To obtain effective and accurate fitting results, the appropriate optimal-order  $m$  and  $n$  are selected by cross-validation. The fitted data are divided into 10 parts to have 10 experiments. One part of the data is chosen as the test group, and the other nine parts of the data are fitted by the ENOPF method, with a different  $m$  and  $n$ . The RMSEs between the fitting results and the test group are calculated. The mean RMSE for each  $m$  and  $n$  is calculated by repeating the abovementioned steps 10 times above so that the order  $m$  and  $n$  of the smaller RMSE can be chosen for fitting.

By fitting with a different  $m$ ,  $n$  will give different fitting results, and with a lower  $m$ ,  $n$  facilitates the use of fewer computational resources. The mean RMSEs corresponding to a specific  $m$  and  $n$  are shown in Figure 3, and the two combinations of each tidal constituent in which the smaller RMSE corresponds to a specific order ( $m_1$  and  $n_1$ ;  $m_2$  and  $n_2$ ) are selected to obtain the cotidal charts (Figures 4 and 5), which are constant for all the parameters tested. As shown in Figures 4 and 5, the two combinations of each tidal constituent are both justified over the whole BYECS and differ in general only in the overlapping area. In order to pick the optimal order, Table 1 lists the mean RMSE of the overlapping area with different  $m$  and  $n$  values. In Figures 4 and 5 and Table 1, the cotidal charts of the optimal order show better consistency and have smaller root-mean-square errors in the

overlapping area. After comprehensive consideration, in Area I, the optimal-order  $m_1$  and  $n_1$  and RMSE of the  $S_a$  constituent are 3, 5, and 7.05 cm, respectively. Moreover, those of the  $S_{sa}$  constituent are 5, 3, and 1.13 cm, respectively. In Area II, the optimal-order  $m_2$  and  $n_2$  and RMSE of the  $S_a$  constituent are 3, 6, and 10.12 cm, respectively. Moreover, that of the  $S_{sa}$  constituent are 3, 2, and 1.48 cm, respectively. Table 2 lists the optimal polynomial order of the ENOPF method for fitting the  $S_a$  and  $S_{sa}$  constituents in the two research areas.

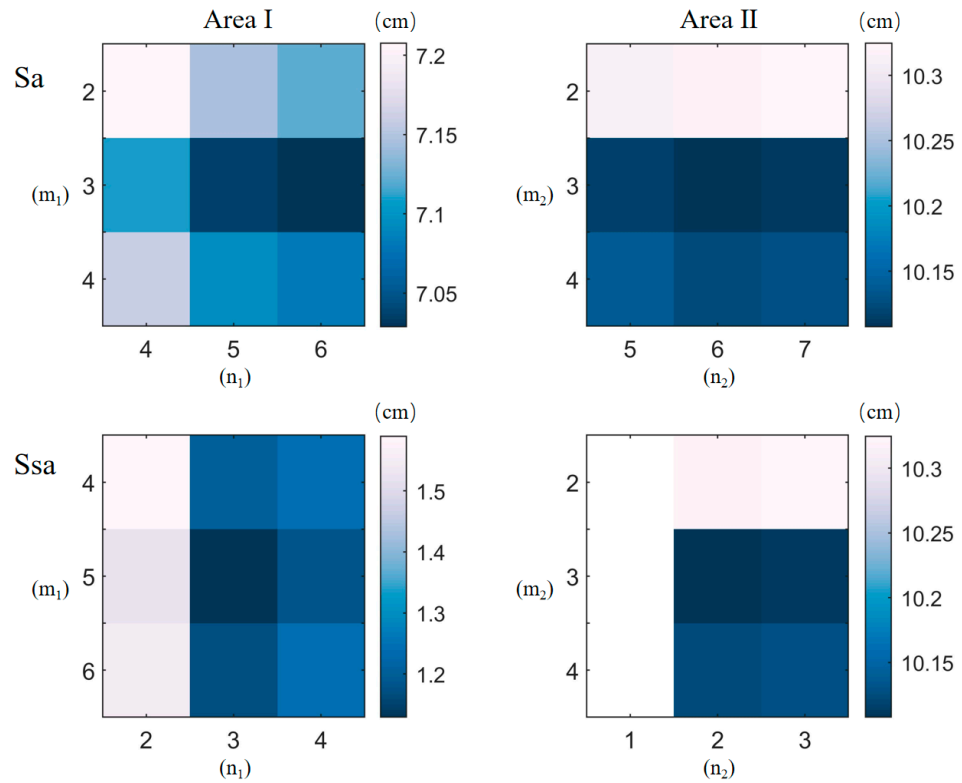


**Figure 3.** The root-mean-square errors (RMSEs) of different orders of equidistant node orthogonal polynomial ( $m$  and  $n$ ) from Area I and Area II.

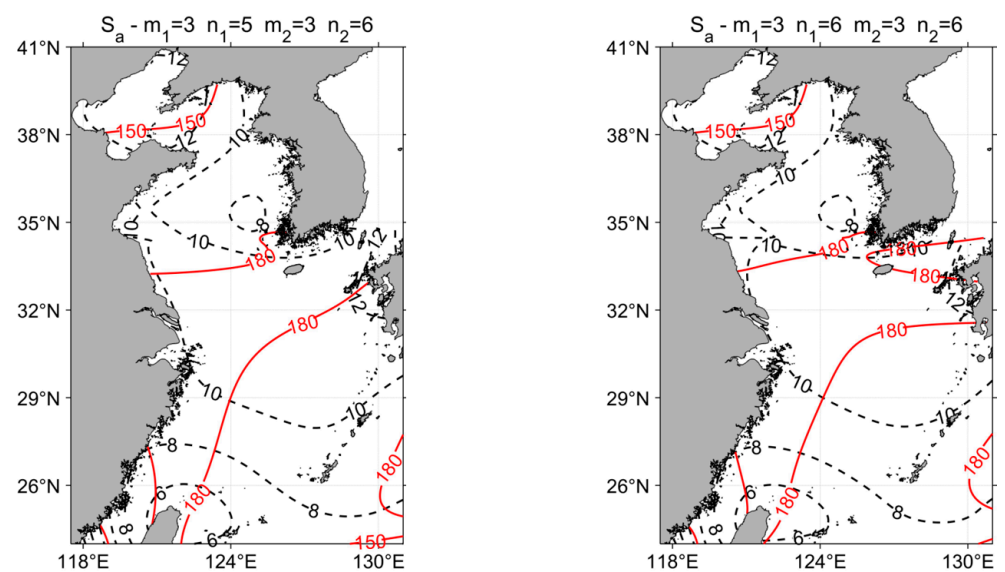


**Figure 4.** The cotidal charts of  $S_a$  constituent with different ( $m_1$  and  $n_1$ ) and ( $m_2$  and  $n_2$ ). Red line: equal phase-lag line. Black line: equal amplitude line.

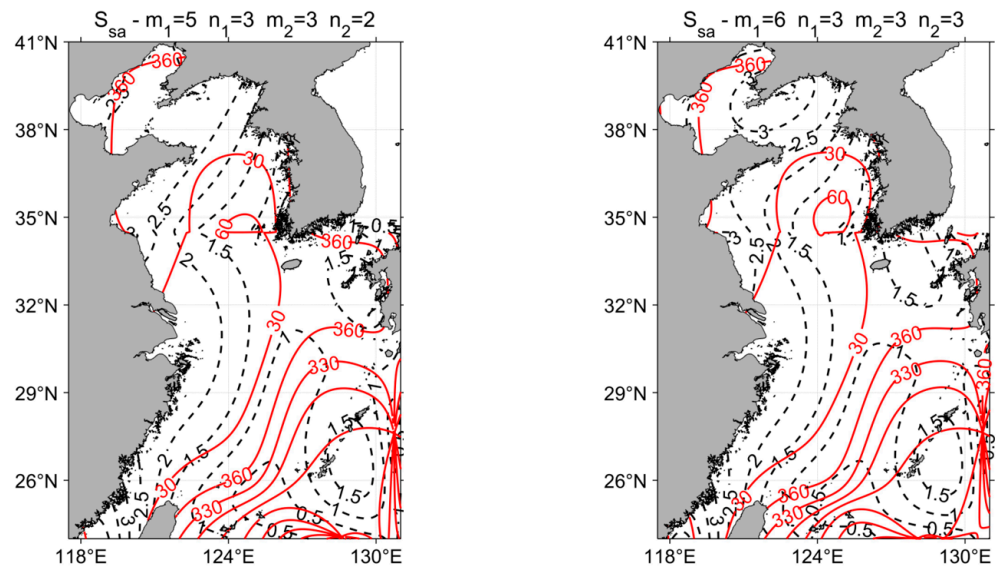


**Figure 5.** The cotidal charts of the  $S_{sa}$  constituent with different  $(m_1 n_1)$  and  $(m_2 n_2)$  values. Red line: equal phase-lag line. Black line: equal amplitude line.

**Table 1.** The root-mean-square errors (RMSEs) of the overlapping area with different orders of equidistant node orthogonal polynomial ( $m$  and  $n$ ) of  $S_a$  and  $S_{sa}$  constituents.

$S_a$ (cm)	$m_2 = 3 n_2 = 5$	$m_2 = 3 n_2 = 6$	$m_2 = 3 n_2 = 7$
$m_1 = 3 n_1 = 5$	0.66	0.62	0.68
$m_1 = 3 n_1 = 6$	0.69	0.70	0.70
$S_{sa}$ (cm)	$m_1 = 5 n_1 = 3$	$m_1 = 5 n_1 = 4$	$m_1 = 6 n_1 = 3$
$m_2 = 3 n_2 = 2$	0.21	0.46	0.48
$m_2 = 3 n_2 = 3$	0.27	0.27	0.21

**Table 2.** The optimal order of the ENOPF for the  $S_a$  and  $S_{sa}$  tidal constituents in the BYECS.

Area I	$S_a$	$S_{sa}$	Area II	$S_a$	$S_{sa}$
$m_1$	3	5	$m_1$	3	3
$n_1$	5	3	$n_2$	6	2

To obtain the harmonic constants of the long-period tidal constituents ( $S_a$  and  $S_{sa}$ ) with higher spatial resolution in the study area, the harmonic constants of the DUACS and T/P satellite altimeter are fitted together in each area. Then, the harmonic constants in Area I and Area II are spliced. Taking  $34.5^\circ\text{N}$  as the dividing line to deal with the overlapping region ( $34\text{--}35^\circ\text{N}$ ). The fitting results of Area I to the south of the dividing line and Area II to the north of the dividing line were reconstructed to form the spatial distribution of the harmonic constant in the whole region. After selection, it was found that the iso-amplitude line and iso-phase-lag line can be well connected in the cotidal charts of the study region.

### 3. Results

#### 3.1. Comparison between Fitted Results and Orbit Data

To verify the feasibility of the fitting results of the ENOPF method, the fitting results obtained by the ENOPF and the other three models are compared with the orbital data (1791 data points). The comparison indexes are RMSE,  $\Delta H$ , and  $\Delta G$ , and the calculation method is as follows:

$$\text{RMSE} = \left\{ \frac{1}{2} \left( H_o^2 + H_s^2 \right) - H_o H_s \cos(G_o - G_s) \right\}^{1/2} \quad (8)$$

where  $H_0$  and  $G_0$  are the actual groups of harmonic constants, and  $H_s$  and  $G_s$  are the processed harmonic constants.

$$\Delta H = \frac{1}{N} \sum_{n=1}^N |H_n - H_n^*|, \Delta G = \frac{1}{N} \sum_{n=1}^N |G_n - G_n^*| \quad (9)$$

where  $H_n$  and  $G_n$  represent the amplitude and phase lag of satellite remote-sensing or tide-gauge data at the  $n$ th point,  $H_n^*$  and  $G_n^*$  are the processed amplitude and phase-lag data at the same point, and  $N$  is the total number of points.

The three indexes are calculated to demonstrate the accuracy of harmonic constants obtained by the ENOPF method in orbital positions and to compare the feasibility of the ENOPF method with the other three models or methods. The average RMSE,  $\Delta H$ , and  $\Delta G$  of the four models or methods are shown in Table 3.

**Table 3.** The root-mean-square errors (RMSEs), amplitude differences ( $\Delta H$ ), and phase-lag differences ( $\Delta G$ ) between the fitting results obtained by the ENOPF method, FES model, EOT20 model, and DUACS data, compared with the X-TRACK data.

RMSE (cm)	ENOPF	DUACS	FES2014	EOT20
$S_a$	1.15	0.93	/	7.19
$S_{sa}$	0.64	0.57	1.27	1.28
$\Delta H$ (cm)	ENOPF	DUACS	FES2014	EOT20
$S_a$	0.85	0.67	/	4.27
$S_{sa}$	0.57	0.54	1.70	1.62
$\Delta G$ (deg)	ENOPF	DUACS	FES2014	EOT20
$S_a$	8.03	6.16	/	81.63
$S_{sa}$	25.91	21.14	52.88	64.36

For the  $S_a$  constituent, the RMSEs of the results of the ENOPF method (1.15 cm) and the DUACS data (0.93 cm) are much lower than those obtained by the EOT20 model (7.19 cm). In terms of the  $\Delta H$  and  $\Delta G$ , the results obtained by the ENOPF method (0.85 cm and  $8.03^\circ$ , respectively) and the DUACS data (0.67 cm and  $6.16^\circ$ , respectively) are lower than those obtained by the EOT20 method (4.27 cm and  $81.63^\circ$ , respectively). For the  $S_{sa}$  constituent, the RMSEs of the results obtained by the ENOPF method (0.64 cm) and the DUACS data (0.57 cm) are lower than those obtained by the other two models (FES2014, 1.27 cm; EOT20, 1.28 cm). In terms of  $\Delta H$  and  $\Delta G$ , the results obtained by the ENOPF method (0.57 cm and  $25.91^\circ$ , respectively) and the DUACS data (0.54 cm and  $21.14^\circ$ , respectively) are lower than those obtained by the other two models (FES2014, 1.70 cm and  $52.88^\circ$ ; EOT20, 1.62 cm and  $64.36^\circ$ , respectively). From the perspective of the three error-evaluation criteria, the results obtained by the ENOPF method and the DUACS data are more consistent, and the errors of the FES2014 model and the EOT20 model are very closed, thus confirming the observations made by Hart-Davis et al. (2021). These results are also an order of magnitude higher than those obtained by the other two models. This may be caused by the lack of data assimilation in the simulation of the long-period tidal constituents by the FES2014 model (Lyard et al. 2021), and the EOT20 model is an improvement compared to the FES2014 model. Therefore, compared with the X-TRACK data, the errors obtained by the FES2014 model and the EOT20 model are larger than those of the ENOPF method and DUACS data.

To show individual differences in orbital errors, the errors of each orbital observation point are shown in Figure 6. For the  $S_a$  constituent, at the orbital observation points, most of the RMSEs of the ENOPF method and the DUACS data are less than 4 cm compared with the orbit data. Meanwhile, most of the RMSEs of the EOT20 model are between 4 cm and 8 cm, making them larger than those of the ENOPF method and the DUACS data. For the  $\Delta H$  and  $\Delta G$ , the errors obtained by the ENOPF method and the DUACS data are less than 2 cm and  $20^\circ$ , respectively. Most of the error scatters of the EOT20 are between

2 cm and 7 cm and between 70° and 120°, respectively. For the  $S_{sa}$  constituent, most of the RMSEs of the ENOPF method and the DUACS data are less than 1.5 cm. Meanwhile, most of the RMSEs obtained by the FES2014 model and the EOT20 model are larger, and most of the error scatters are below 2.5 cm. The regression analysis of the calculated errors is used to obtain a more accurate error distribution, which is shown in Figure 7. The error scatter plot and error-distribution diagram indicate that the ENOPF method is relatively the most effective of the four models and methods, no matter the  $S_a$  or the  $S_{sa}$  constituent.

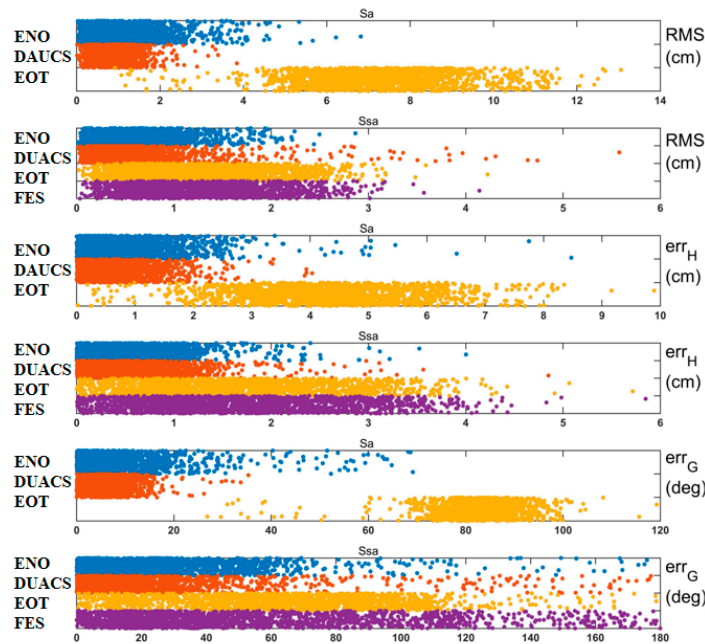


**Figure 6.** Error scatter plot of fitting results obtained by ENOPF method, FES2014 model, EOT20 model, and DUACS data, compared with X-TRACK data. ENOPF Method: blue dots. DUACS data: orange dots. EOT20 model: yellow dots. FES2014 model: purple dots.

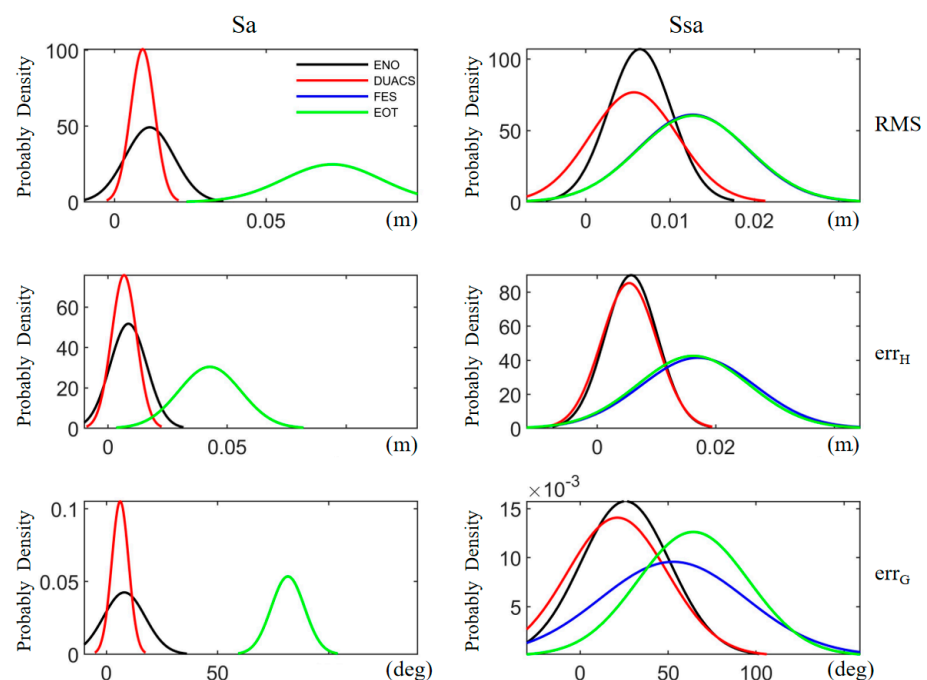


**Figure 7.** Error-distribution diagram of fitting results obtained by ENOPF method, FES2014 model, EOT20 model, and DUACS data, compared with X-TRACK data. ENOPF method: black line. DUACS data: red line. FES2014 model: blue line. EOT20 model: green line.

### 3.2. Comparison between Fitted Results and the Tide Gauges

To further verify the fitting accuracy of the ENOPF method, the results of the ENOPF method, FES2014 model, EOT20 model, and DUACS data were compared with the harmonic constants observed by the 62 tide gauges. For comparison with observations, the harmonic constants of four methods or models at the location of the 62 tide gauges were obtained via linear interpolation. The average RMSE,  $\Delta H$ , and  $\Delta G$  are listed in Table 4 to compare the advantages and disadvantages of the four methods or models.

**Table 4.** The root-mean-square errors (RMSEs), amplitude differences ( $\Delta H$ ), and phase-lag differences ( $\Delta G$ ) obtained from the fitting results obtained by the ENOPF method, FES2014 model, EOT20 model, and DUACS data, compared with the data of tide gauges.

RMSE (cm)	ENOPF	DUACS	FES2014	EOT20
$S_a$	6.19	6.85	/	13.53
$S_{sa}$	1.10	1.21	1.24	1.34
$\Delta H$ (cm)	ENOPF	DUACS	FES2014	EOT20
$S_a$	5.85	6.44	/	11.55
$S_{sa}$	0.72	0.83	1.69	1.55
$\Delta G$ (deg)	ENOPF	DUACS	FES2014	EOT20
$S_a$	25.44	28.79	/	101.41
$S_{sa}$	59.09	76.16	107.56	150.88

For the  $S_a$  constituent, the RMSEs of the three methods or models are similar to those obtained by comparing with X-TRACK data. The RMSEs of the ENOPF method (6.19 cm) and the DUACS data (6.85 cm) are lower than the RMSEs of the EOT20 method (13.53 cm). In terms of  $\Delta H$  and  $\Delta G$ , the results of the ENOPF method (5.85 cm and 25.44°, respectively) and the DUACS data (6.44 cm and 28.79°, respectively) are lower than those of the EOT20 model (11.55 cm and 101.41°, respectively). For the  $S_{sa}$  constituent, the errors between the results of the four methods or models and observations of the tide gauges are similar. The RMSE of the ENOPF method is the smallest (1.10 cm) and slightly smaller than that obtained by the other three models (DUACS, 1.21 cm; FES2014, 1.24 cm; and EOT20, 1.34 cm). The  $\Delta H$  and  $\Delta G$  of the ENOPF method are the smallest (0.72 cm and 59.09°, respectively) and slightly smaller than those obtained by the other three models (DUACS, 0.83 cm and 76.16°; FES2014, 1.69 cm and 107.56°; and EOT20, 1.55 cm and 150.88°). Because all positions of the 62 tide gauges are located in the shallow sea, with a complex terrain and close distance to the coast, this error is mainly caused by the systematic error between the T/P satellite altimeter data and the tide gauge data. The RMSE,  $\Delta H$ , and  $\Delta G$  are 13.59 cm, 12.29 cm, and 74.62°, respectively, and the error obtained by comparing with the tide gauges is larger than that obtained by comparing with the X-TRACK data.

For showing individual differences of the RMSE,  $\Delta H$ , and  $\Delta G$  of different tide gauges, the errors of each tide gauge are shown in Figure 8. For the  $S_a$  constituent, the scatter plot shows that most of the RMSEs of the ENOPF method and the DUACS data are less than 10 cm when compared with the tide gauges. Meanwhile, most of the RMSEs of the EOT20 model are larger than those of the above two methods, where most of the RMSEs are below 15 cm. For the  $\Delta H$  and  $\Delta G$ , the scatter plot shows that by using the ENOPF method and the DUACS data, most of the  $\Delta H$  and  $\Delta G$  values are less than 10 cm and 40°, respectively. However, most of the scatter points of the EOT20 model have larger errors, and most of the error scatters are less than 20 cm and 120°, respectively. For the  $S_{sa}$  constituent, there are only observations of 28 tidal stations, so the error scatters are less than that of the  $S_a$  constituent. Most of the RMSEs of the four methods or models are between 1 cm and 2.5 cm, and most of the amplitude difference points are less than 2 cm. The phase-lag differences' scatters of the EOT20 model are distributed far away, between 120° and 160°, while the phase-lag differences' scatters of the other three models are distributed between 60° and

100°. To further analyze the distributions of errors, the regression analysis of the error is shown in Figure 9. The results display that the harmonic constants obtained by the ENOPF method are in agreement with the observations of the tide gauges.

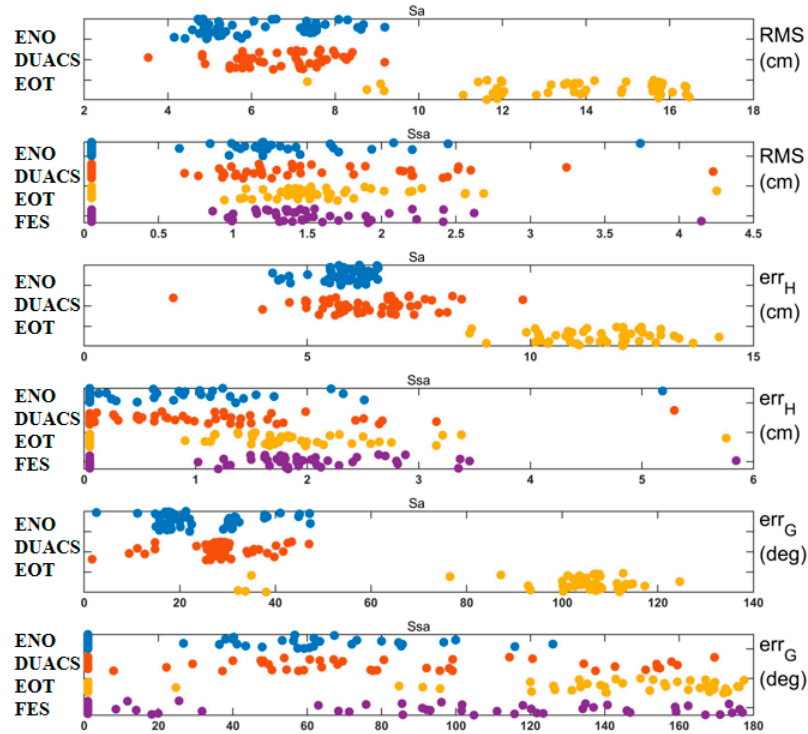


**Figure 8.** Error scatter plot of fitting results obtained by ENOPF method, FES2014 model, EOT20 model, and DUACS data, compared with the data of tide gauges. ENOPF method: blue dots. DUACS data, orange dots. EOT20 model, yellow dots. FES2014 model: purple dots.

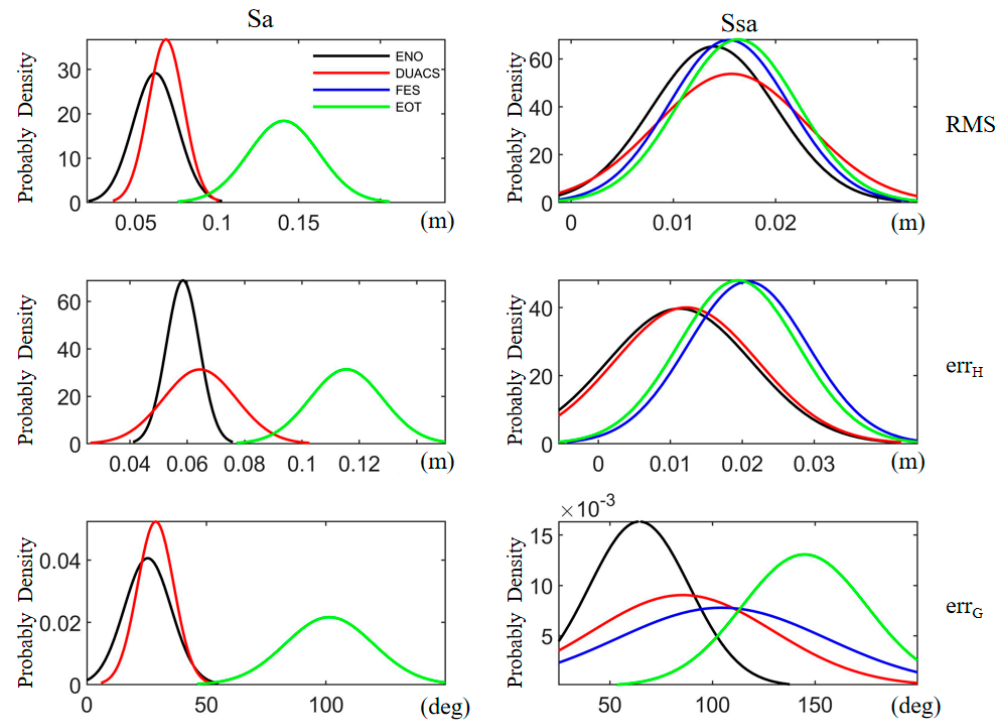


**Figure 9.** Error-distribution diagram of fitting results obtained by ENOPF method, FES2014 model, EOT20 model, and DUACS data, compared with tide gauges. ENOPF method: black line. DUACS data: red line. FES2014 model: blue line. EOT20 model: green line.

These results show that, as a tool to extract the harmonic constant from satellite altimeter data, the ENOPF method is feasible and accurate.

#### 4. Discussion

To compare the full-field fitting result with a resolution of  $2' \times 2'$  ( $3.42 \text{ km}^2$ ) of the ENOPF method, the cotidal charts of the  $S_a$  and  $S_{sa}$  constituents obtained by four methods or models are shown in Figures 10 and 11, and the distribution of amplitude differences and phase-lag differences obtained by methods or models compared with X-TRACK data are shown in Figures 12 and 13.

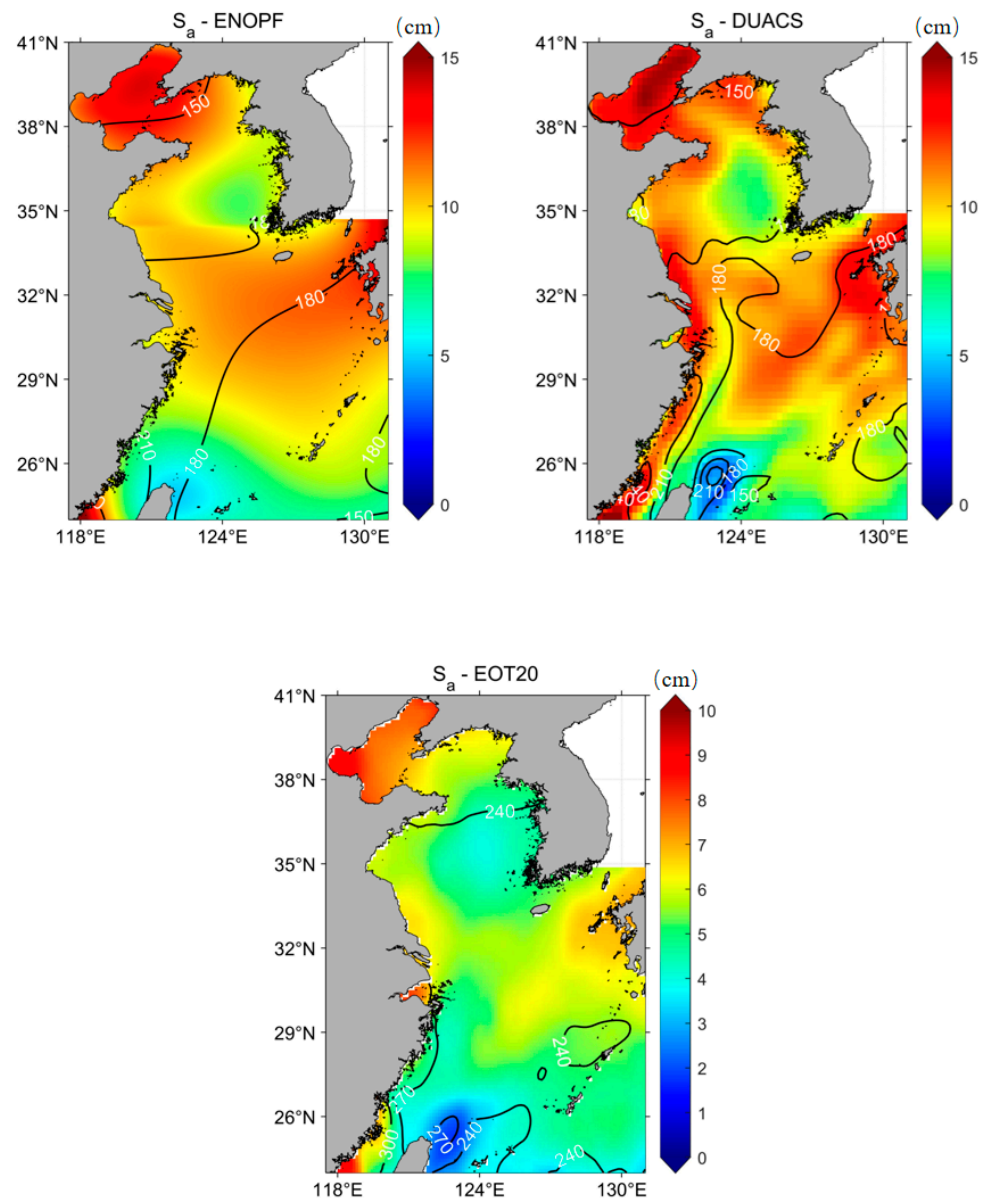


**Figure 10.** The cotidal charts of  $S_a$  constituent obtained by the ENOPF method, EOT20 model, and DUACS data.

For the  $S_a$  constituent, from the perspective of amplitude distribution, the large amplitude of the four methods or models is distributed in the northwest part of the study area, which is consistent with the satellite altimeter amplitude data. The maximum amplitude of the EOT20 model is 10 cm, which has a large difference with the X-TRACK amplitude data. The maximum amplitude of the ENOPF method and DUACS data is about 15 cm, which is consistent with the actual observed results. As seen in Figure 12, the results show

that the ENOPF method and DUACS data have a better fitting effect on the amplitude data in the study area than the EOT20 model, and they perform well for the fitting results in the offshore area. From the perspective of phase-lag distribution, the ENOPF method and DUACS data distribution in the study area are generally consistent with the satellite altimeter phase-lag data. For the EOT20 model, the phase-lag data are smoother than those of the FES2014 model. However, from Figure 13, we can see that the cotidal chart obtained by the FES2014 model is still quite different from the X-TRACK amplitude data, indicating that the ENOPF method and DUACS data also have a good fitting effect in the study area of the phase-lag data, and they both perform well in the Bohai Sea and the Yellow Sea. The phase-lag data obtained from DUACS data vary greatly in the southwest part of the study area, and the distribution of the phase-lag data in the study region is slightly different from that of the X-TRACK amplitude data.

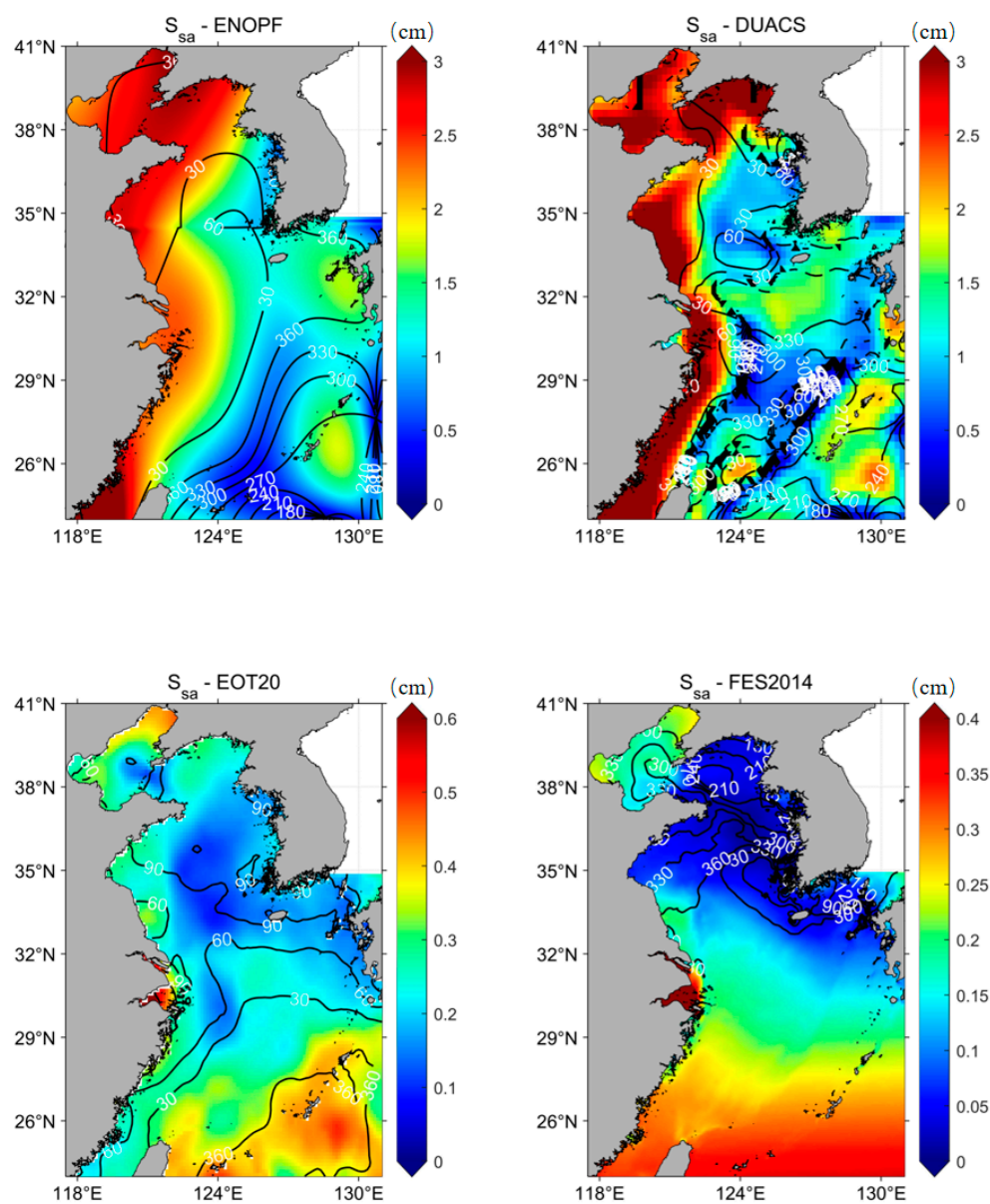


**Figure 11.** The cotidal charts of  $S_{sa}$  constituent obtained by the ENOPF method, EOT20 model, FES2014 model, and DUACS data.

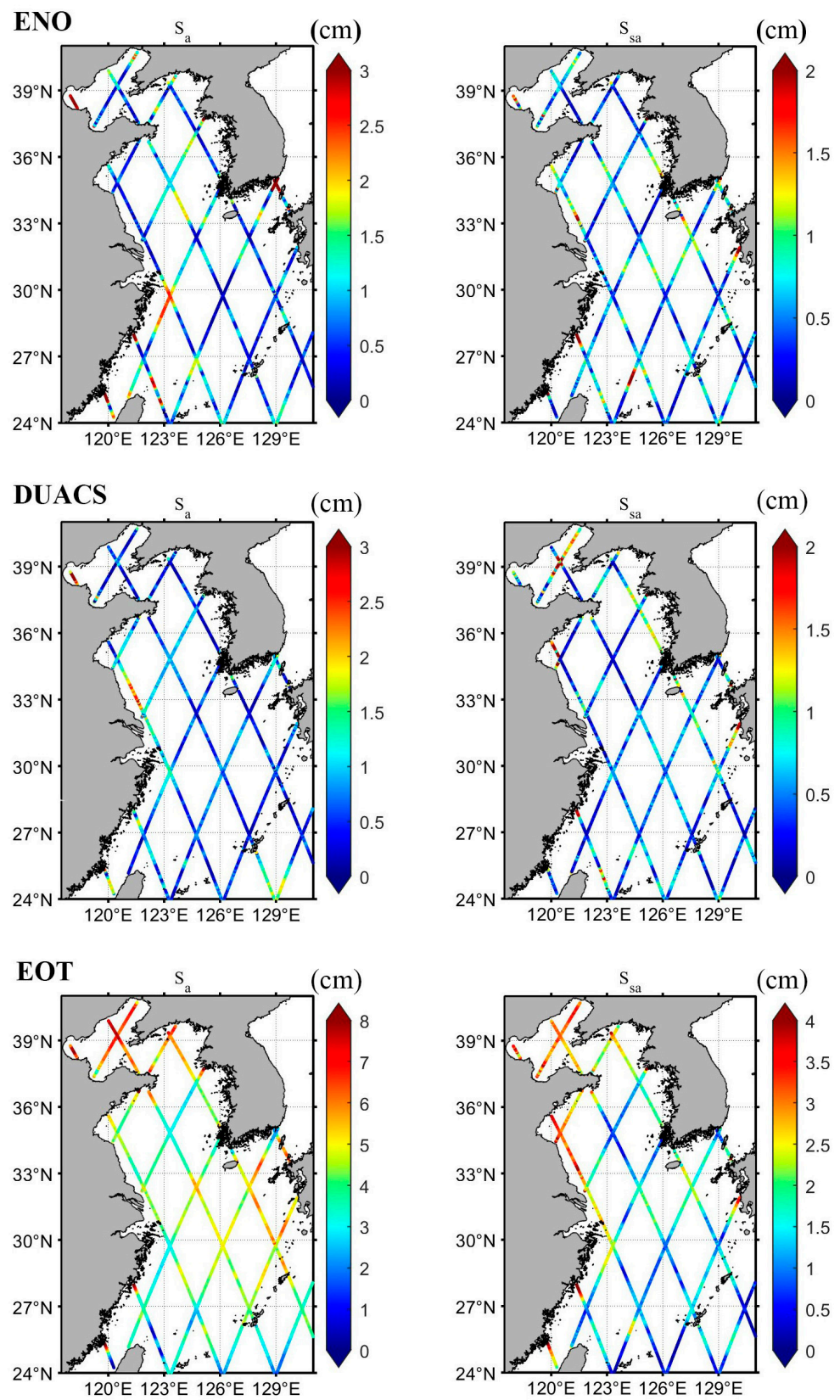


**Figure 12.** The distribution of amplitude differences obtained by ENOPF method, DUACS data, and EOT20 model, compared with X-TRACK data.

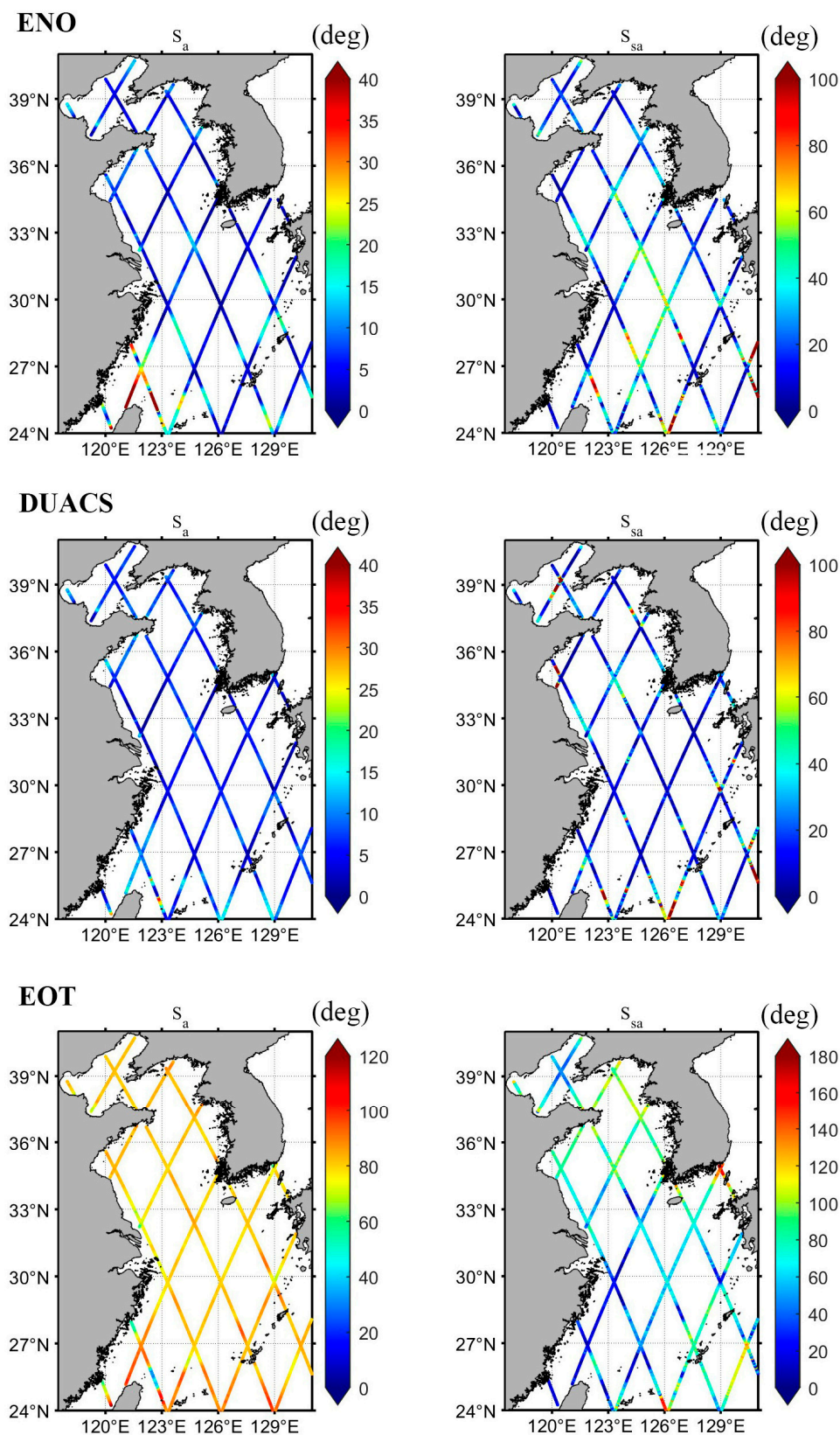


**Figure 13.** The distribution of phase-lag differences obtained by ENOPF method, DUACS data, and EOT20 model, compared with X-TRACK data.

For the  $S_{sa}$  constituent, from the perspective of amplitude distribution, the large amplitude of the FES2014 model and EOT20 model is distributed in the southern part of the

study area, while the large amplitude of the ENOPF method and DUACS data is distributed in the western part of the study area. The amplitude data obtained by the ENOPF method and DUACS data are in good agreement with the actual satellite data. From the perspective of phase-lag distribution, the phase lag of the DUACS and FES2014 have a lot of high frequency information, while the phase lag of the EOT20 model and ENOPF method is smooth compared with the previous two methods. From Figures 12 and 13, it can also be found that the ENOPF method and DUACS data perform well in the study region.

In general, the ENOPF method has good accuracy in the study area, and the harmonic constants of the  $S_a$  and the  $S_{sa}$  constituents are consistent with the satellite altimeter data. Moreover, compared with the FES2014 model with a  $1/16^\circ$  resolution, the EOT20 model with a  $1/8^\circ$  resolution, and DUACS data with a  $15' \times 15'$  resolution, the ENOPF method is characterized by improving the resolution infinitely. As shown in Figures 10 and 11, the resolution of the ENOPF method is significantly improved compared with that of the DUACS data, indicating that the ENOPF method can obtain a higher-resolution cotidal chart and is reliable in fitting harmonic constants.

## 5. Conclusions

In this paper, the ENOPF method was employed to fit the T/P satellite altimeter data and DUACS data of two long-period tidal constituents ( $S_a$  and  $S_{sa}$ ) to obtain the harmonic constants field in the BYECS. The ENOPF method saves a lot of computing resources because it does not need to consider the effects of many uncertain parameters, and this method can increase the resolution as much as necessary. Since the terrain in the area ( $34^\circ\text{--}35^\circ\text{N}$ ,  $117.5^\circ\text{--}131^\circ\text{E}$ ) of this landform undulates drastically, the study area was divided into two parts, and the optimal-order  $m$  and  $n$  of the two parts were determined by cross-validation. Then, the full-field harmonic constant fitted by the ENOPF method was obtained by splicing the two areas.

To verify the validity of the ENOPF method, the harmonic constants of the ENOPF method, FES2014 model, EOT20 model, and DUACS data were compared with 1791 data points of the X-TRACK data. The RMSEs, amplitude differences, and phase-lag differences (1.15 cm, 0.85 cm,  $8.03^\circ$ ; 0.64 cm, 0.57 cm,  $25.91^\circ$ , respectively) of the ENOPF method are smaller than those of the FES2014 model, and for the EOT20 model, they are little bit bigger than they are for the DUACS data in the  $S_a$  constituent. The harmonic constants of the four methods or models are also compared with those of the 62 tide gauges in the study area. By comparison, the error of the ENOPF method is smaller than the other three methods or models, the RMSEs, amplitude differences, and phase-lag differences are 6.19 cm, 5.85 cm, and  $25.44^\circ$ ; and 1.10 cm, 0.72 cm, and  $59.09^\circ$ , respectively. The distribution of harmonic constant in the full field obtained by ENOPF is close to the actual satellite data. The comparison of the cotidal charts of four methods or models indicates that the results of the ENOPF method are more reasonable in the study region. The ENOPF method can effectively obtain the harmonic constant field of the long-period tidal constituents in the BYECS. The future work should focus on addressing the fitting in the nearshore conditions and in the deeper water conditions, including some physical processes in the fitting process as much as possible.

**Author Contributions:** Y.Z. (Yunfei Zhang), conceptualization, data curation, formal analysis, investigation, methodology, validation, writing—original draft, and writing—review and editing; Q.W., conceptualization, software, methodology, writing—review and editing, and investigation; Y.Z. (Yibo Zhang), conceptualization, data curation, validation, software, and writing—review and editing; M.X., data curation, methodology, software, and writing—review and editing; Y.W., conceptualization, funding acquisition, methodology, project administration, and resources; X.L., formal analysis, methodology, project administration, and resources. All authors have read and agreed to the published version of the manuscript.

**Funding:** This work was supported by the National Key Research and Development Project of China, through grant 2019YFC1408405; and the National Natural Science Foundation of China, through grants U2006210.

**Data Availability Statement:** DUACS altimeter data are available from the Copernicus Marine Service (<https://marine.copernicus.eu>, accessed on 1 May 2023). The TOPEX/Poseidon (T/P) altimeter data were provided by the National Aeronautics and Space Administration (NASA) (<http://marine.copernicus.eu/servicesportfolio/access-to-products/>, accessed on 1 May 2023). The tidal harmonic constants of X-TRACK (DOI: 10.6096/CTOH\_XTRACK\_Tidal\_2018\_01, accessed on 1 May 2023) were provided by the AVISO+ (<https://www.aviso.altimetry.fr/en/data/products/auxiliary-products/coastal-tide-xtrack.html>, accessed on 1 May 2023). The data of the tide gauges were provided by the Korea Hydrographic and Oceanographic Agency (<http://www.khoa.go.kr/oceangrid/gis/category/observe/observeSearch.do>, accessed on 1 May 2023). The tidal harmonic constants from the FES2014 are available at <https://www.aviso.altimetry.fr/> (accessed on 1 May 2023). The tidal harmonic constants from EOT20 are available at <https://doi.org/10.17882/79489> (accessed on 1 May 2023).

**Acknowledgments:** We deeply thank Xianqing Lv for his constructive suggestions on the manuscript.

**Conflicts of Interest:** The authors declare no conflict of interest.

## References

- Munk, W.; Wunsch, C. Abyssal Recipes II: Energetics of Tidal and Wind Mixing. *Deep. Sea Res. Part I Oceanogr. Res. Pap.* **1998**, *45*, 1977–2010. [[CrossRef](#)]
- Cook, S.E.; Lippmann, T.C.; Irish, J.D. Modeling Nonlinear Tidal Evolution in an Energetic Estuary. *Ocean Model.* **2019**, *136*, 13–27. [[CrossRef](#)]
- Fang, G. Dissipation of Tidal Energy in Yellow Sea. *Oceanol. Limnol. Sin.* **1979**, *10*, 200–213.
- Haigh, I.D.; Pickering, M.D.; Green, J.A.M.; Arbic, B.K.; Arns, A.; Dangendorf, S.; Hill, D.F.; Horsburgh, K.; Howard, T.; Idier, D.; et al. The Tides They Are A-Changin’: A Comprehensive Review of Past and Future Nonastronomical Changes in Tides, Their Driving Mechanisms, and Future Implications. *Rev. Geophys.* **2020**, *58*, e2018RG000636. [[CrossRef](#)]
- Bu, J.; Yu, K.; Park, H.; Huang, W.; Han, S.; Yan, Q.; Qian, N.; Lin, Y. Estimation of Swell Height Using Spaceborne GNSS-R Data from Eight CYGNSS Satellites. *Remote Sens.* **2022**, *14*, 4634. [[CrossRef](#)]
- Li, W.; Cardellach, E.; Fabra, F.; Ribo, S.; Rius, A. Assessment of Spaceborne GNSS-R Ocean Altimetry Performance Using CYGNSS Mission Raw Data. *IEEE Trans. Geosci. Remote Sens.* **2020**, *58*, 238–250. [[CrossRef](#)]
- Peng, Q.; Jin, S. Significant Wave Height Estimation from Space-Borne Cyclone-GNSS Reflectometry. *Remote Sens.* **2019**, *11*, 584. [[CrossRef](#)]
- Guillou, N.; Chapalain, G. Numerical Simulation of Tide-Induced Transport of Heterogeneous Sediments in the English Channel. *Cont. Shelf Res.* **2010**, *30*, 806–819. [[CrossRef](#)]
- Bao, X.; Gao, G.; Yan, J. Three Dimensional Simulation of Tide and Tidal Current Characteristics in the East China Sea. *Oceanol. Acta* **2001**, *24*, 135–149. [[CrossRef](#)]
- Niwa, Y.; Hibiya, T. Three-Dimensional Numerical Simulation of M2 Internal Tides in the East China Sea. *J. Geophys. Res. Ocean.* **2004**, *109*. [[CrossRef](#)]
- Cao, A.; Guo, Z.; Lü, X. Inversion of Two-Dimensional Tidal Open Boundary Conditions of M2 Constituent in the Bohai and Yellow Seas. *Chin. J. Oceanol. Limnol.* **2012**, *30*, 868–875. [[CrossRef](#)]
- Teng, F.; Fang, G.; Xu, X. Effects of Internal Tidal Dissipation and Self-Attraction and Loading on Semidiurnal Tides in the Bohai Sea, Yellow Sea and East China Sea: A Numerical Study. *Chin. J. Oceanol. Limnol.* **2017**, *35*, 987–1001. [[CrossRef](#)]
- Guo, X.; Yanagi, T. Three-Dimensional Structure of Tidal Current in the East China Sea and the Yellow Sea. *J. Oceanogr.* **1998**, *54*, 651–668. [[CrossRef](#)]
- Zheng, J.; Mao, X.; Lv, X.; Jiang, W. The M2 Cotidal Chart in the Bohai, Yellow, and East China Seas from Dynamically Constrained Interpolation. *J. Atmos. Ocean. Technol.* **2020**, *37*, 1219–1229. [[CrossRef](#)]
- Kuh Kang, S.; Lee, S.-R.; Lie, H.-J. Fine Grid Tidal Modeling of the Yellow and East China Seas. *Cont. Shelf Res.* **1998**, *18*, 739–772. [[CrossRef](#)]
- Andersen, O.B. Shallow Water Tides in the Northwest European Shelf Region from TOPEX/POSEIDON Altimetry. *J. Geophys. Res. Oceans* **1999**, *104*, 7729–7741. [[CrossRef](#)]
- He, Y.; Lu, X.; Qiu, Z.; Zhao, J. Shallow Water Tidal Constituents in the Bohai Sea and the Yellow Sea from a Numerical Adjoint Model with TOPEX/POSEIDON Altimeter Data. *Cont. Shelf Res.* **2004**, *24*, 1521–1529. [[CrossRef](#)]
- Gill, S.K.; Schultz, J.R. (Eds.) *Tidal Datums and Their Applications*; NOAA Special Publication NOS CO-OPS 1 ; NOAA, NOS Center for Operational Oceanographic Products and Services: Silver Spring, MD, USA, 2001. [[CrossRef](#)]
- Guohong, F. Tide and tidal current charts for the marginal seas adjacent to China. *Chin. J. Oceanol. Limnol.* **1986**, *4*, 1–16. [[CrossRef](#)]
- Smith, A.J.E.; Ambrosius, B.A.C.; Wakker, K.F.; Woodworth, P.L.; Vassie, J.M. Ocean tides from harmonic and response analysis on TOPEX/POSEIDON altimetry. *Adv. Space Res.* **1998**, *22*, 1541–1548. [[CrossRef](#)]
- Piccioni, G.; Dettmering, D.; Schwatke, C.; Passaro, M.; Seitz, F. Design and Regional Assessment of an Empirical Tidal Model Based on FES2014 and Coastal Altimetry. *Adv. Space Res.* **2021**, *68*, 1013–1022. [[CrossRef](#)]

22. Deng, X.; Featherstone, W.E. A Coastal Retracking System for Satellite Radar Altimeter Waveforms: Application to ERS-2 around Australia. *J. Geophys. Res. Oceans* **2006**, *111*. [[CrossRef](#)]
23. Roblou, L.; Lyard, F.; le Henaff, M.; Maraldi, C. X-Track, a New Processing Tool for Altimetry in Coastal Oceans. In Proceedings of the International Geoscience and Remote Sensing Symposium (IGARSS), Barcelona, Spain, 23–28 July 2007; pp. 5129–5133.
24. Birol, F.; Léger, F.; Passaro, M.; Cazenave, A.; Niño, F.; Calafat, F.M.; Shaw, A.; Legeais, J.F.; Gouzenes, Y.; Schwatke, C.; et al. The X-TRACK/ALES Multi-Mission Processing System: New Advances in Altimetry towards the Coast. *Adv. Space Res.* **2021**, *67*, 2398–2415. [[CrossRef](#)]
25. Lyard, F.H.; Allain, D.J.; Cancet, M.; Carrère, L.; Picot, N. FES2014 Global Ocean Tide Atlas: Design and Performance. *Ocean. Sci.* **2021**, *17*, 615–649. [[CrossRef](#)]
26. Hart-Davis, M.G.; Piccioni, G.; Dettmering, D.; Schwatke, C.; Passaro, M.; Seitz, F. EOT20: A Global Ocean Tide Model from Multi-Mission Satellite Altimetry. *Earth Syst. Sci. Data* **2021**, *13*, 3869–3884. [[CrossRef](#)]
27. Ray, R.D.; Erofeeva, S.Y. Long-Period Tidal Variations in the Length of Day. *J. Geophys. Res. Solid Earth* **2014**, *119*, 1498–1509. [[CrossRef](#)]
28. Cartwright, D.E.; Tayler, R.J. New Computations of the Tide-generating Potential. *Geophys. J. R. Astron. Soc.* **1971**, *23*, 45–73. [[CrossRef](#)]
29. Woodworth, P.L. A Note on the Nodal Tide in Sea Level Records. *J. Coast. Res.* **2012**, *28*, 316–323. [[CrossRef](#)]
30. Ponte, R.M.; Chaudhuri, A.H.; Vinogradov, S.V. Long-Period Tides in an Atmospherically Driven, Stratified Ocean. *J. Phys. Oceanogr.* **2015**, *45*, 1917–1928. [[CrossRef](#)]
31. Kantha, L.H.; Stewart, J.S.; Desai, S.D. Long-Period Lunar Fortnightly and Monthly Ocean Tides. *J. Geophys. Res. Oceans* **1998**, *103*, 12639–12647. [[CrossRef](#)]
32. Wunsch, C.; Haidvogel, D.B.; Iskandarani, M.; Hughes, R. Dynamics of the Long-Period Tides. *Prog. Oceanogr.* **1997**, *40*, 81–108. [[CrossRef](#)]
33. Lee, E.J.; Kim, K.; Park, J.H. Reconstruction of Long-Term Sea-Level Data Gaps of Tide Gauge Records Using a Neural Network Operator. *Front. Mar. Sci.* **2022**, *9*, 1037697. [[CrossRef](#)]
34. Xu, M.; Wang, Y.; Wang, S.; Lv, X.; Chen, X. Ocean Tides near Hawaii from Satellite Altimeter Data. Part I. *J. Atmos. Ocean. Technol.* **2021**, *38*, 937–949. [[CrossRef](#)]
35. Wang, Q.; Zhang, Y.; Wang, Y.; Xu, M.; Lv, X. Fitting Cotidal Charts of Eight Major Tidal Components in the Bohai Sea, Yellow Sea Based on Chebyshev Polynomial Method. *J. Mar. Sci. Eng.* **2022**, *10*, 1219. [[CrossRef](#)]
36. Wang, Y.; Zhang, Y.; Xu, M.; Wang, Y.; Lv, X. Ocean Tides near Hawaii from Satellite Altimeter Data. Part II. *J. Atmos. Ocean. Technol.* **2022**, *39*, 1015–1029. [[CrossRef](#)]
37. Romero, M.; de Madrid, A.P.; Mañoso, C.; Vinagre, B.M. IIR Approximations to the Fractional Differentiator/Integrator Using Chebyshev Polynomials Theory. *ISA Trans.* **2013**, *52*, 461–468. [[CrossRef](#)] [[PubMed](#)]
38. Hu, X.-Y.; Yu, X.-H. The Chebyshev Polynomial Fitting Properties of Discrete Cosine Transform. *Signal Process. Image Commun.* **1998**, *13*, 15–20. [[CrossRef](#)]

**Disclaimer/Publisher’s Note:** The statements, opinions and data contained in all publications are solely those of the individual author(s) and contributor(s) and not of MDPI and/or the editor(s). MDPI and/or the editor(s) disclaim responsibility for any injury to people or property resulting from any ideas, methods, instructions or products referred to in the content.